Journal of Pharmaceutical Analysis 13 (2023) 603–615

Contents lists available at ScienceDirect

Journal of Pharmaceutical Analysis

journal homepage: www.elsevier.com/locate/jpa

Original article

Cocktail hepatocarcinoma therapy by a super-assembled nano-pill targeting XPO1 and ATR synergistically

Liuyun Gong [a, 1], Yinliang Lu [a, 1], Jing Wang [a], Xinyue Li [a], Jing Zhao [c], Yuetong Chen [a], Rongze Ma [a], Jinlu Ma [a], Tianya Liu [b, **], Suxia Han [a, *]

[a] Department of Radiation Oncology, The First Affiliated Hospital of Xi'an Jiaotong University, Xi'an, 710061, China
[b] National & Local Joint Engineering Research Center of Biodiagnosis and Biotherapy, The Second Affiliated Hospital of Xi'an Jiaotong University, Xi'an, 710004, China
[c] Department of Radiotherapy, The First Affiliated Hospital Soochow University, Suzhou, Jiangsu, 215000, China

ARTICLE INFO

Article history:
Received 19 March 2023
Received in revised form
19 April 2023
Accepted 24 April 2023
Available online 28 April 2023

Keywords:
Liver cancer
Drug combination
Cancer therapy
ATR inhibitor
XPO1 inhibitor

ABSTRACT

Intensive cancer treatment with drug combination is widely exploited in the clinic but suffers from inconsistent pharmacokinetics among different therapeutic agents. To overcome it, the emerging nanomedicine offers an unparalleled opportunity for encapsulating multiple drugs in a nano-carrier. Herein, a two-step super-assembled strategy was performed to unify the pharmacokinetics of a peptide and a small molecular compound. In this proof-of-concept study, the bioinformatics analysis firstly revealed the potential synergies towards hepatoma therapy for the associative inhibition of exportin 1 (XPO1) and ataxia telangiectasia mutated-Rad3-related (ATR), and then a super-assembled nano-pill (gold nano drug carrier loaded AZD6738 and 97–110 amino acids of apoptin (AP) (AA@G)) was constructed through camouflaging AZD6738 (ATR small-molecule inhibitor)-binding human serum albumin onto the AP-Au supramolecular nanoparticle. As expected, both in vitro and in vivo experiment results verified that the AA@G possessed extraordinary biocompatibility and enhanced therapeutic effect through inducing cell cycle arrest, promoting DNA damage and inhibiting DNA repair of hepatoma cell. This work not only provides a co-delivery strategy for intensive liver cancer treatment with the clinical translational potential, but develops a common approach to unify the pharmacokinetics of peptide and small-molecular compounds, thereby extending the scope of drugs for developing the advanced combination therapy.

1. Introduction

As one of the most lethal malignancies worldwide, liver cancer causes very low five-year survival less than 1/5 in the past few years [1]. Although some successes have been achieved in the field of targeted therapy of hepatocellular carcinoma, few of them provide prominent survival benefits due to the typical physiological complexity of liver cancer [2,3]. As a result, the monotherapy or the stand-alone therapy may suffer from the compensatory resistance quickly [4–6]. To overcome it, the emerging combination therapy, with respect to the simultaneous dosage of multiple therapeutic agents, provides a clinical method to synergistically regulate different signaling pathways, therefore enhance therapeutic effect and overcome drug resistance [7,8], thereby prolonging the survival of the patients and decreasing undesirable side effects [9–11]. Towards the optimized combination therapy, two general strategies have emerged: elucidating the specific mechanisms underlying activities to discover new drug combinations, and developing novel drug combination systems to give full play to their remarkable medicinal effects.

As for the discovery of new therapeutic combinations against liver cancer, we focused on a eukaryotic nuclear-cytoplasmic exporter termed exportin 1 (XPO1) and ataxia telangiectasia mutated-Rad3-related (ATR). The nuclear localization signal and nuclear export signal (NES) are core signatures of proteins for controlling nuclear-cytoplasmic transport. XPO1 is a eukaryotic nuclear-cytoplasmic exporter that binds directly to proteins harboring NES and translocates them to the cytoplasm [12]. XPO1

Peer review under responsibility of Xi'an Jiaotong University.
* Corresponding author.
** Corresponding author.
E-mail addresses: tianyaliu@xjtu.edu.cn (T. Liu), shan87@xjtu.edu.cn (S. Han).
[1] Both authors contributed equally to this work.

https://doi.org/10.1016/j.jpha.2023.04.017

over-expresses in multiple cancers and is a validated drug target [13]. However, tumor recurrence and metastasis are often happening in patients because of tumor heterogeneity and rapid adaptation to targeted therapies [14,15]. Inoue et al. [16] prove that tumor cells response to XPO1 inhibitor-induced DNA damage can recover because cell cycle arrest facilitates DNA damage repair. Therefore, XPO1 inhibitor combine with other DNA damage response drugs which targeting cell cycle may improve the therapeutic effect of liver cancer. DNA damage response signaling pathway is launched with the activation of ATR [17], which are essential for homologous recombination (HR) DNA damage repair [18]. For these reasons, we hypothesize that the XPO1 inhibition combined with the ATR suppression might contribute to the more effective medicines to fight against liver cancer.

As for the drug combination systems, the traditional cocktail regimen through several independent drug administration always suffers from respective pharmacokinetic profiles of each single drug with different tendency of biodistribution and circulation, resulting in the attenuated outcomes of the combination therapy [7,19]. To overcome it, the nanomedicine provided a feasible and clinical strategy to develop drug combination cocktail, by which multiple therapeutic agents can be assembled and/or encapsulated into one nanoparticle, thereby unifying the pharmacokinetic property of loading drugs [20,21]. Among them, some gold nanoparticles derived nanomedicines have been applied in clinical trials, due to their intrinsic inertion in physiological environment [22–26]. Moreover, as non-toxic carrier for anti-cancer drugs, gold nanoparticles display the enhancive accumulation in tumor sites via enhanced permeability and retention effect [27–30] and deep tumor penetration capacity through loosening extracellular matrix of tumors [31]. Herein, we de novo design a drug combination system to simultaneously target XPO1 by a 16-mer peptide (97–110 amino acids of apoptin, AP) and ATR by a small-molecule inhibitor named AZD6738 in hepatoma carcinoma cells. In details, a super-assembled nano-pill (gold nano drug carrier loaded AZD6738 and AP (AA@G)) was constructed through camouflaging AZD6738 (ATR small-molecule inhibitor)-binding human serum albumin (HSA) onto the AP (XPO1 peptide inhibitor)-Au supramolecular nanoparticle. Expectedly, both in vitro and in vivo experiment results demonstrated that the AA@G possessed the extraordinary biocompatibility and enhanced therapeutic effect through inducing cell cycle arrest, promoting DNA damage and inhibiting DNA repair of hepatoma cell. Collectively, this work not only provides a co-delivery strategy for intensive liver cancer treatment with the clinical translational potential, but develops a common approach to unify the pharmacokinetics of peptide and small-molecular compounds, thereby extending the scope of drugs for developing the advanced combination therapy.

2. Materials and methods

2.1. Materials

AP (RVSELKESLITTTPSC) was obtained from China Peptides Co., Ltd. (Xi'an, China). All other chemicals used in this study were purchased from Sigma-Aldrich (Sigma-Aldrich, St. Louis, MO, USA) unless otherwise specified. The γ-H2AX antibody (No. 97148), CyclinD1 antibody (No. 55506), ATR antibody (No.2851), p-chk1 antibody (No. 2348) and Tubulin antibody (No. 5335) were purchased from Cell Signaling Technology Inc. (Boston, MA, USA). The Rad51 antibody (No. ab213) was purchased from abcam (Cambridge, UK). Acetonitrile and water (high performance liquid chromatography (HPLC) grade) were purchased from Fisher Scientific Ltd. (Xi'an, China).

2.2. Cell culture

The liver cancer cell lines of Hepg2, Huh7, Hep3B and Hep1-6 were purchased from American Type Culture Collection and cultured in Dulbecco's modified eagle medium. They then supplemented with 10% fetal bovine serum (Biological Industries Israel Beit-Haemek, Kibbutz Beit-Haemek, Israel) and 1% penicillin-streptomycin (Gibco, New York City, NY, USA). Cells were grown in a 5% CO_2 incubator at 37 °C.

2.3. Animals

Athymic C57BL/6 mice were purchased from the Beijing Experimental Animal Center (Beijing, China) and maintained in a specific pathogen-free facility approved by the Laboratory Animal Center of Xi'an Jiaotong University (Xi'an, China). All animal procedures below were conducted in accordance with the Guidelines for the Care and Use of Laboratory Animals, and were approved by the Department of Medicine, Xi'an Jiaotong University (Approval No.: 2021-1756).

2.4. The design and synthesis of AA@G

For HSA-ATR inhibitor synthesis, 1 mg of tris (2-carboxyethyl) phosphine hydrochloride was first added to 0.5 mL of HSA (10 mg/mL) solution. Then, ATR inhibitor (1 mM) was added to the above HSA solution. Last, 5 mL of ultra-pure water was used to dilute solution. For gold nano drug carrier loaded AP (AP@G) synthesis, first, gold nano-adjuvant solution was synthesized as previous studies [23,26,27]. Briefly, 0.5 mL of chloroauric acid solution (10 mM) was added to 4.5 mL of 2-[4-(2-hydroxyethyl)-L-piperazinyl] ethane sulfonic (HEPES, 50 mM) acid buffer, stirring under heating conditions until the solution turns purple red, indicating the successful preparation of gold nano-adjuvant solution. After 2.5 mg of AP, 2 mg of NH_2-PEG_{2000}-SH and 4.5 mL of HEPES (50 mM) were mixed well, 0.5 mL of chloroauric acid solution (10 mM) was added and kept stirring until the solution turns pale yellow into colorless, marking the formation of AP@G. Finally, 2 mL of HSA-ATR inhibitor solution, 2 mL of AP@G solution and 4 mL of gold nano-adjuvant solution was mixed for 10 min, and the gold nano drug carrier loaded AZD6738 and AP (AA@G) was completely prepared.

2.5. Drug release

HPLC analysis was performed to evaluate drug loading efficiency using an Agilent 1100 LC System (Agilent Technologies, Santa Clara, CA, USA) and C_{18} column (Phenomenex, Los Angeles, CA, USA). All samples were dissolved in acetonitrile:water (9:1, *V*/*V*) with 0.1% (*V*/*V*) trifluoroacetic acid added as a stabilizer. Before injection, all samples were filtered through a 0.45-μm syringe filter. The release kinetics of AP and AZD6738 were conducted using Slide-A-Lyzer™ MINI dialysis devices (molecular weight 20,000; Xi'an, China). Briefly, 2 mg of AA@G was dispersed in phosphate buffered saline (PBS, pH 7.4 and 6.0, respectively) with or without glutathione (GSH). The samples were shaken under 200 rpm at room temperature. Aliquots were taken from the dialysis bag at specified time points (0, 2, 12, 13, 14, 16, 20, and 24 h), and the release of AP and AZD6738 into the buffer solution was detected via HPLC.

2.6. Cellular uptake analysis

This section was referred to our previous article [32]. Cells were treated with AA@G (0.2 mg/mL), which were loaded with Cy5. Cells

treated with AP and AZD6738 compound without gold nano adjuvant were used as a control. After incubation for 6 h, the cells were washed three times with cold PBS and the treated cells were harvested for flow cytometry analysis.

2.7. In vitro therapeutic effect and drug synergy analysis

The cytotoxicity against Hepg2, Huh7, Hep3B and Hep1-6 cells was measured by cell counting kit-8 (CCK8) assay, as shown in our previous article [32]. The q value of drug combined efficacy was calculated by Jin's formula: $q = E_{A+B}/(E_A + E_B - E_A \times E_B)$, where E_{A+B} is the inhibition rate of the combination of two drugs, E_A and E_B are the inhibition rates of each single drug, $q < 1$ indicates that two drugs has antagonistic effect, and $q \geq 1$ indicates that two drugs has synergistic effect. The coefficient of drug interaction (CDI) was calculated according to the formula: CDI = AB/(A × B). AB is the ratio of absorbance value between the two drug combination groups and the control group, and A or B is the ratio of absorbance value between the single drug group and the control group. When CDI < 1, the two drugs have synergy effect, and when CDI < 0.7, the synergistic effect is very significant.

2.8. Cell cycle and apoptosis analysis

Prepare cell samples refer to our previous article [32]. Apoptosis kit and cycle kit were purchased on Becton, Dickinson and Company (Franklin, NJ, USA), and used for analyzing cell apoptosis and cell cycle according to the instruction.

2.9. Western blotting (WB)

Cells were seeded in 6-well plates and divided into three groups and added PBS, gold nano drug carrier (@G) and AA@G respectively for 48 h. Cells were harvested and resuspended in lysis buffer, washed thrice with ice-cold PBS and lysed in extraction buffer (40 mmol/L Tris-HCl, pH 7.5, 150 mmol/L KCl, 1 mmol/L ethylenediamine tetraacetic acid, 1% Triton X-100, 100 mmol/L $NaVO_3$, 1 mmol/L phenylmethanesulfonyl fluoride) supplemented with the protease inhibitor cocktail. Proteins were subjected to WB assay as described previously [32].

2.10. Immunofluorescence

After culturing cells, cells were fixed with 4% paraformaldehyde, permeabilized in 0.2% Triton X-100, blocked in 3% bovine serum

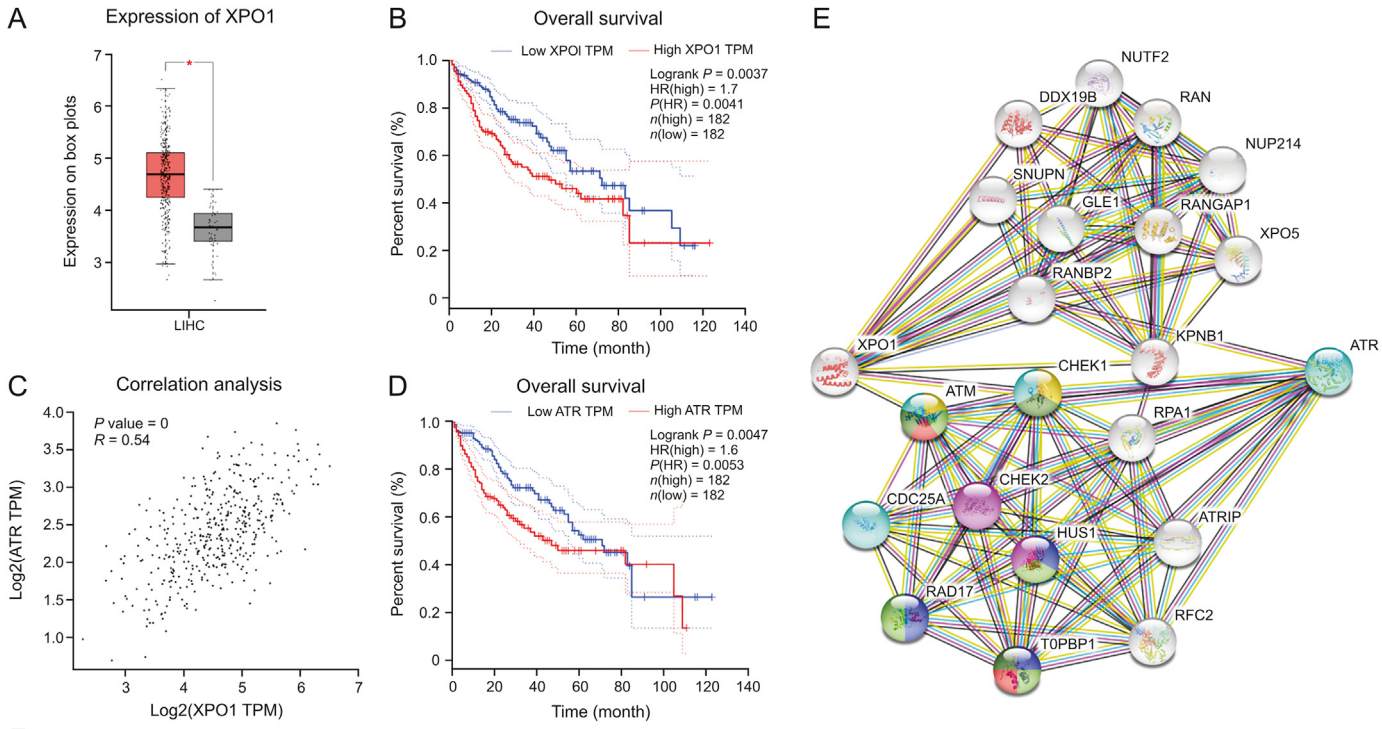

F

ID	Gene ontology/KEGG analysis	Strength	False discovery rate
GO:0072425	Signal transduction involved in G_2 DNA damage checkpoint	2.17	0.0092
GO:0044818	Mitotic G_2/M transition checkpoint	2.07	1.26×10^{-5}
GO:0031573	Intra-S-phase DNA damage checkpoint	2.05	0.0142
GO:0007095	Mitotic G_2 DNA damage checkpoint	1.93	0.0212
GO:0031572	G_2 DNA damage checkpoint	1.92	0.00089
hsa04110	Cell cycle	1.47	0.00086

Fig. 1. Bioinformatics analysis of exportin 1 (XPO1) and ataxia telangiectasia mutated-Rad3-related (ATR). (A) Different expression of XPO1 between liver cancer samples ($n = 69$) and normal samples ($n = 50$). LIHC: liver cancer and health control. (B) Overall survival between low XPO1 expression samples and high XPO1 expression samples. (C) Correlation analysis of XPO1 and ATR. (D) Overall survival between low ATR expression samples and high ATR expression samples. (E) Functional protein association network of XPO1 and ATR. (F) Gene Ontology (GO) and Kyoto Encyclopedia of Genes and Genomes (KEGG) analysis of proteins in Fig. 1E. TPM: transcripts per kilobase of exon model per million mapped reads.

albumin, and incubated with primary anti-p-chk1, anti-Rad51, anti-γ-H2AX and anti-CyclinD1 antibody for 1 h and fluorescent-conjugated secondary antibody (Invitrogen, Paisley, UK) for 1 h. Then, cells were washed and stained with Actin-Tracker (30 min) and 4',6-diamidino-2-phenylindole (DAPI, 3 min). The images of the cells were obtained by laser confocal microscopy (Actin-Tracker, excitation: 488 nm; DAPI, excitation: 400 nm, and fluorescent-conjugated antibody, excitation: 594 nm).

2.11. In vivo safety evaluation

For the biosafety evaluation, female C57BL/6 mice were randomLy divided into five groups (control, @G, AP@G, gold nano drug carrier loaded AZD6738 (AT@G) and AA@G), four groups were injected with 200 μL of drugs (0.2 mg/mL) via abdomen every daily for five days, while the control group was injected with the same amount of PBS. The mice were sacrificed, and blood was collected after 30 days. Blood routine examination and biochemistry and inflammatory factors analyses were performed, and the major organs (heart, liver, spleen, lungs, and kidneys) were weighed and collected for hematoxylin-eosin staining (H&E) staining.

2.12. Therapeutic effect in vivo

Mice were divided into 1) control; 2) @G; 3) AP@G; 4) AT@G, and 5) AA@G groups after bearing-tumor reached about 100 mm^3. The drugs were intravenously injected into the abdomen every daily for five days. The length and width of the treated tumors were measured using a vernier caliper every two days. Tumor size was measured with calipers using formula $V = (a \times b^2)/2$, in which a and b are the

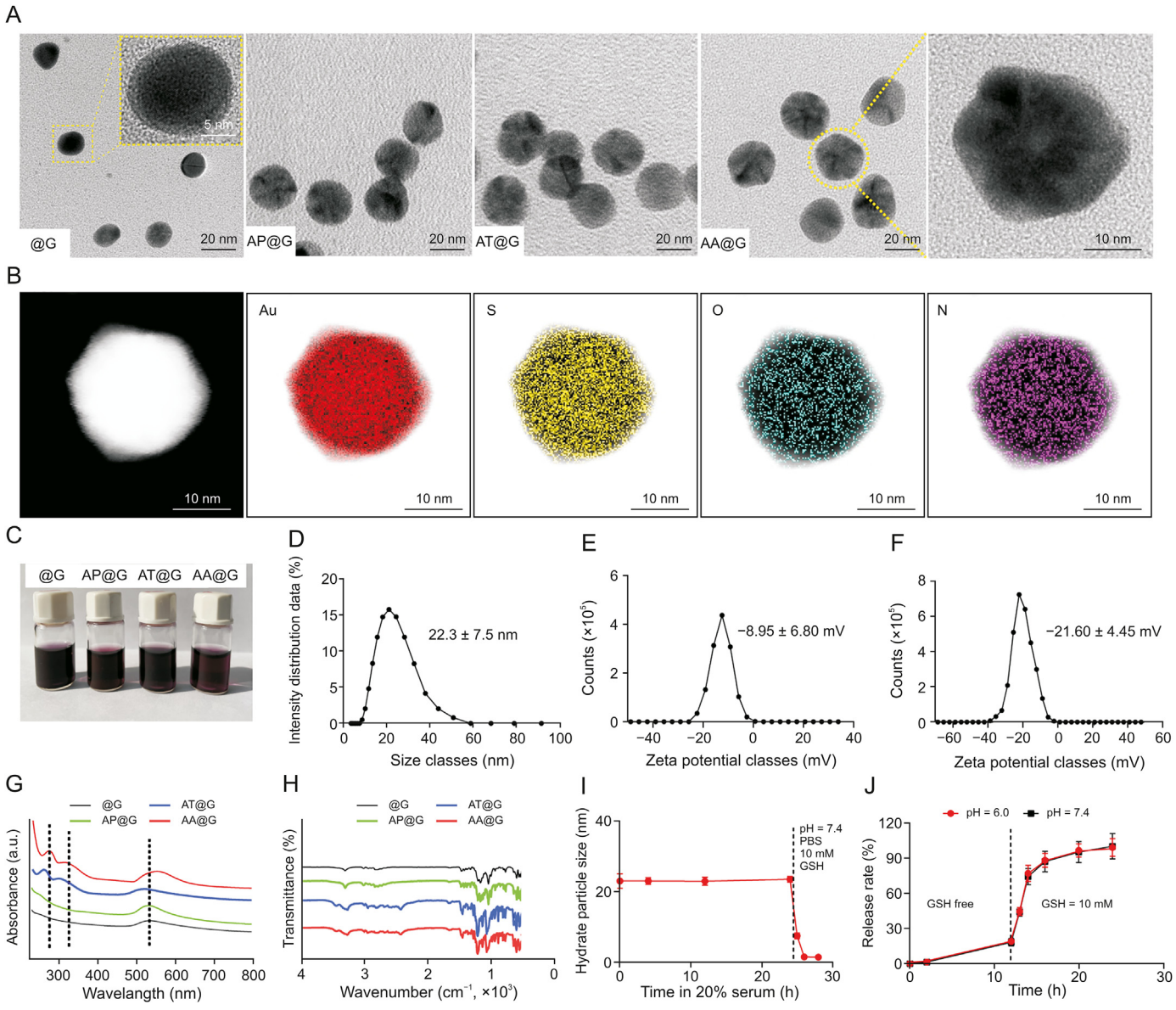

Fig. 2. Characterization of gold nano drug carrier loaded AZD6738 and 97–110 amino acids of apoptin (AP) (AA@G). (A) Transmission electron microscope pictures of gold nano drug carrier (@G), gold nano drug carrier loaded AP (AP@G), gold nano drug carrier loaded AZD6738 (AT@G) and gold nano drug carrier loaded AZD6738 and AP (AA@G). (B) Element mapping for AA@G. (C) Photograph of @G, AP@G, AT@G and AA@G. (D) Hydrated particle size of AA@G captured by dynamic light scattering. Zeta potentials of (E) @G and (F) AA@G. (G) The ultraviolet-visible spectroscopy (UV-vis) of @G, AP@G, AT@G and AA@G. (H) Fourier transform infrared spectroscopy analysis of @G, AP@G, AT@G and AA@G. (I) Changes of hydrodynamic diameter of AA@G in phosphate buffered saline (PBS) with or without glutathione (GSH) for different time ($n = 3$). (J) AP release profile in different time and conditions ($n = 3$).

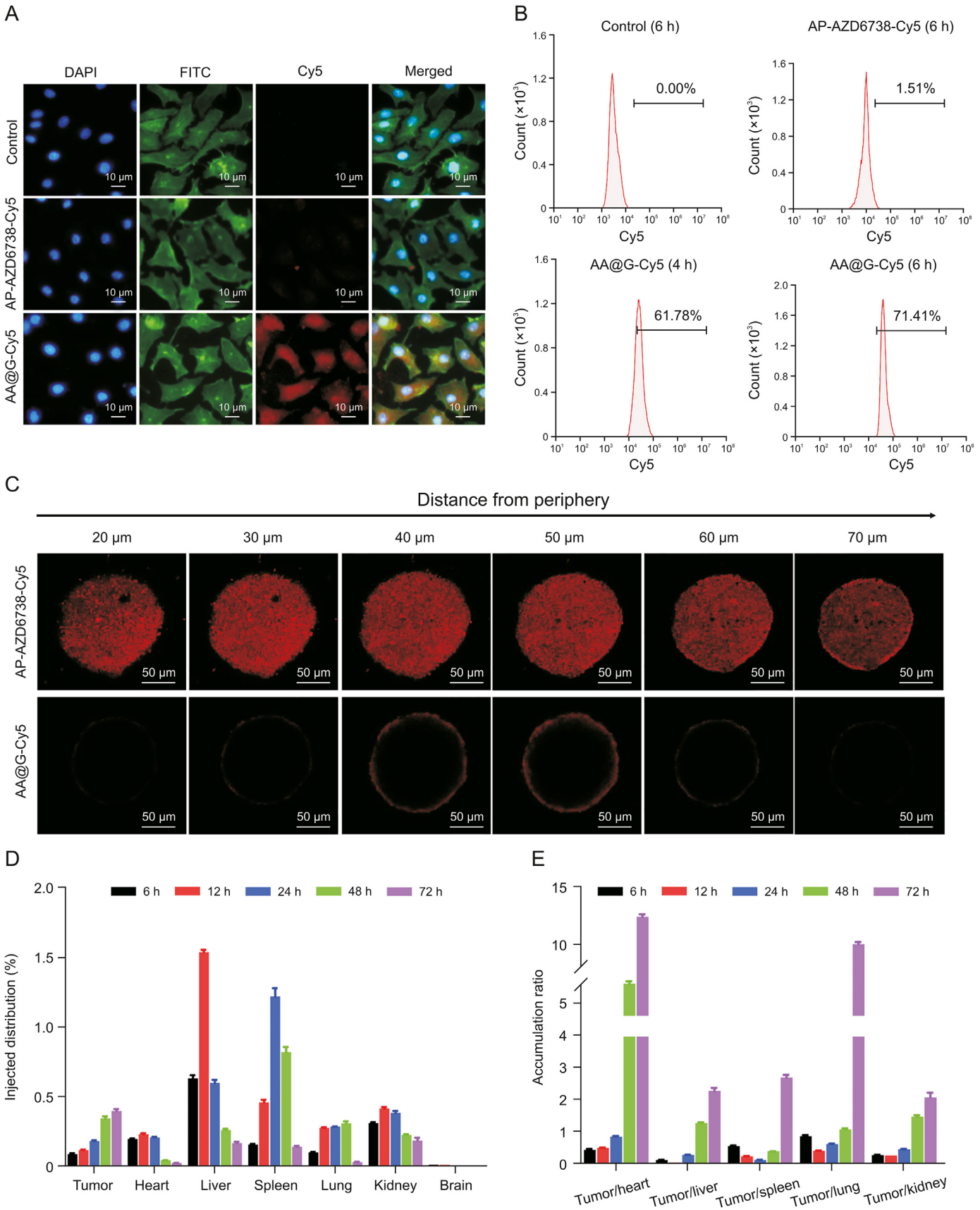

Fig. 3. Gold nano drug carrier loaded AZD6738 and 97–110 amino acids of apoptin (AP) (AA@G) targeting ability. (A) Confocal imaging of AA@G incubated with Hep3B cancer cells. (B) Flow cytometry analysis results of intracellular AA@G fluorescence for different time. (C) Confocal *Z*-stack results of AA@G penetration in 3D Hep3B cell spheroids. Color red indicates Cy5-labeled AA@G. (D) Inductively coupled plasma-mass spectrometry result of AA@G content in different organs ($n = 3$). (E) The tumor-to-organ distribution ratio of AA@G ($n = 3$). DAPI: 4′,6-diamidino-2-phenylindole; FITC: Fluoresceine isothiocyanate.

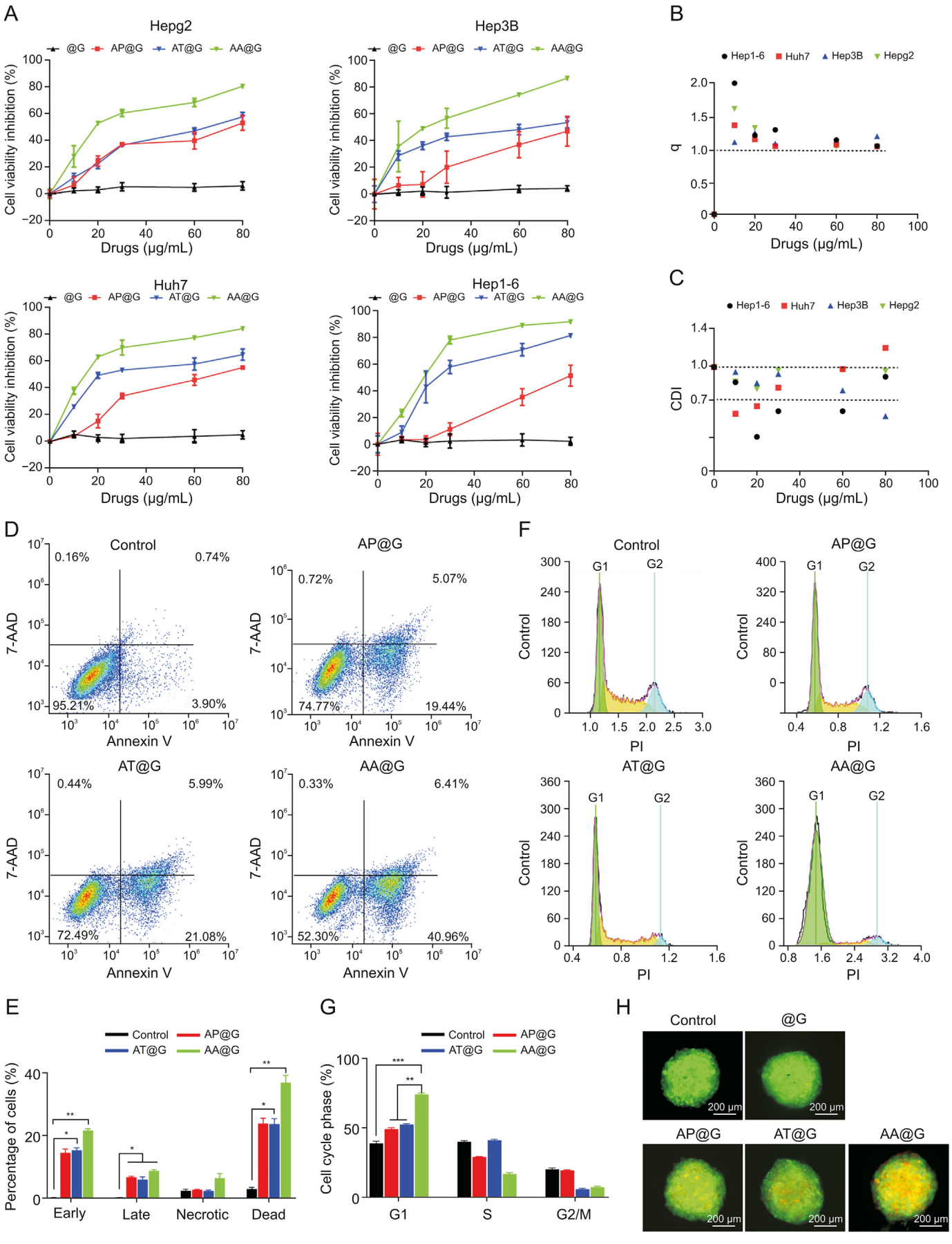
A
Hepg2
Hep3B
Huh7
Hep1-6
@G
AP@G
AT@G
AA@G
Cell viability inhibition (%)
Drugs (μg/mL)
B
Hep1-6
Huh7
Hep3B
Hepg2
q
Drugs (μg/mL)
C
CDI
Drugs (μg/mL)
D
Control
AP@G
AT@G
AA@G
7-AAD
Annexin V
0.16%
0.74%
95.21%
3.90%
0.72%
5.07%
74.77%
19.44%
0.44%
5.99%
72.49%
21.08%
0.33%
6.41%
52.30%
40.96%
F
Control
AP@G
AT@G
AA@G
G1
G2
PI
E
Control
AP@G
AT@G
AA@G
Percentage of cells (%)
Early
Late
Necrotic
Dead
G
Cell cycle phase (%)
G1
S
G2/M
H
Control
@G
AP@G
AT@G
AA@G
200 μm

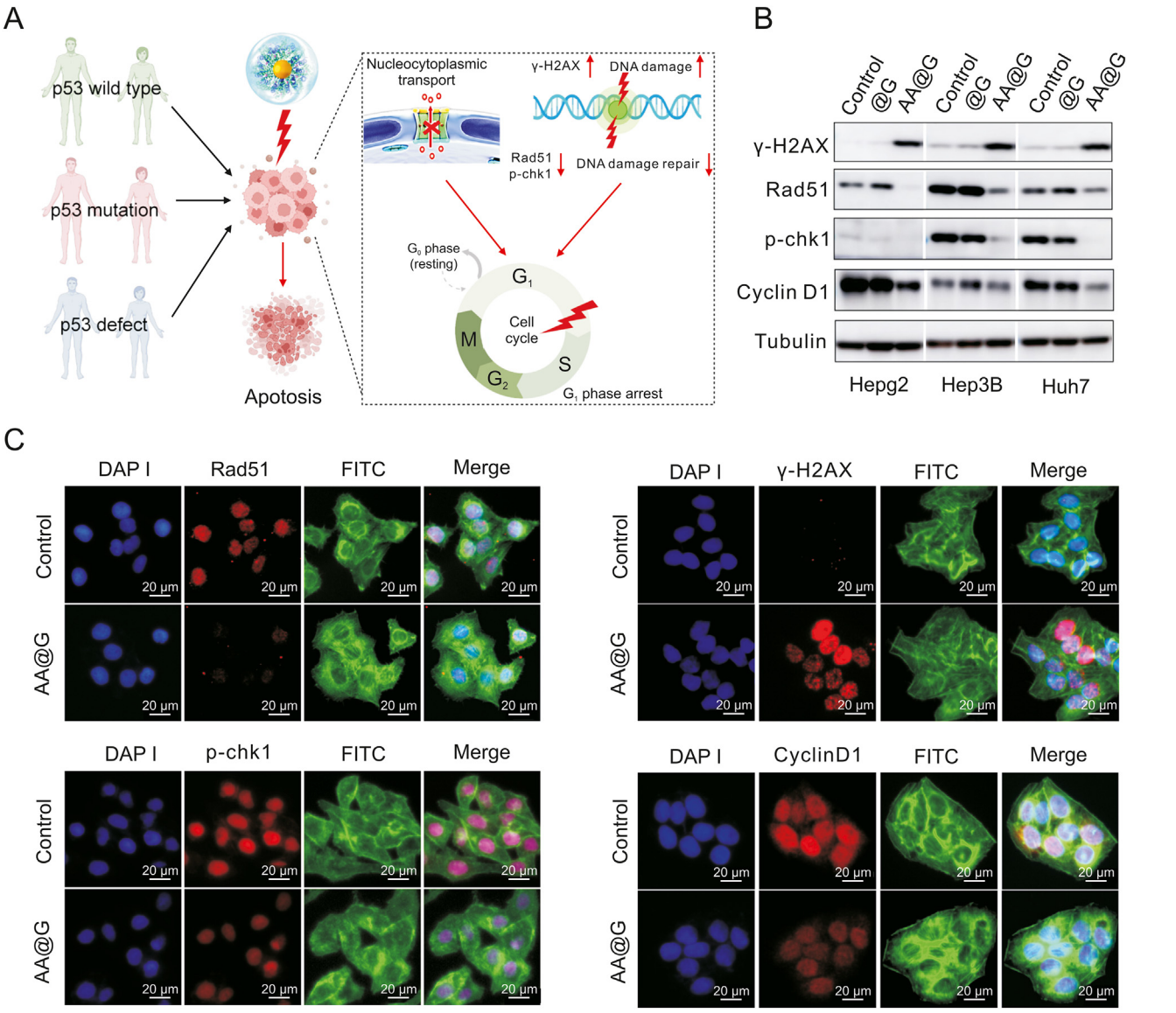

Fig. 5. Therapeutic mechanism of gold nano drug carrier loaded AZD6738 and 97–110 amino acids of apoptin (AP) (AA@G) in vitro. (A) Schematic diagram of therapeutic mechanism of AA@G. (B) Expression levels of γ-H2AX, Rad51, p-chk1 and CyclinD1 detected by Western blot. (C) Immunofluorescence experiment for expression levels of γ-H2AX, Rad51, p-chk1, and CyclinD1. DAPI: 4′,6-diamidino-2-phenylindole; FITC: fluoresceine isothiocyanate.

largest and the smallest perpendicular diameters, respectively. Bearing-tumors in every group were followed individually until they measured greater than 1000 mm^3. The animals were sacrificed. The samples were submerged in formalin for histological analysis.

2.13. Bioinformatics analysis

Gene expression profiling interactive analysis (GEPIA, http://gepia.cancer-pku.cn) is an open web server for analyzing RNA-sequencing expression data of 9,736 tumors and 8,587 normal samples from The Cancer Genome Atlas and Genotype-Tissue Expression projects, using a standard processing pipeline [33]. The expression of XPO1 in liver cancer samples compared to normal samples, the overall survival in high or low XPO1 and ATR expression samples, and the correlation between XPO1 and ATR and were analyzed with GEPIA. Search tool for the retrieval of interacting genes (STRING) (https://string-db.org/cgi/input.pl) is an online tool that for predicting protein association network of

Fig. 4. Therapeutic efficacy of gold nano drug carrier loaded AZD6738 and 97–110 amino acids of apoptin (AP) (AA@G) in vitro. (A) Cell counting Kit-8 (CCK-8) assay results. (B) Combined drug effect of AP and AZD6738. (C) Drug synergy of AP and AZD6738. (D) Apoptosis analysis results. (E) Cell cycle analysis results. (F) Quantification results of Fig. 4D ($n = 3$). (G) Quantification of cell cycle analysis in Fig. 4E ($n = 3$). (H) Calcein-AM/propidium iodide staining analysis. Green fluorescence represents living cells and red fluorescence represents dead cell. $^{*}P < 0.05$; $^{**}P < 0.01$; and $^{***}P < 0.001$. CDI: coefficient of drug interaction; 7-AAD: 7-aminoactinomycin D.

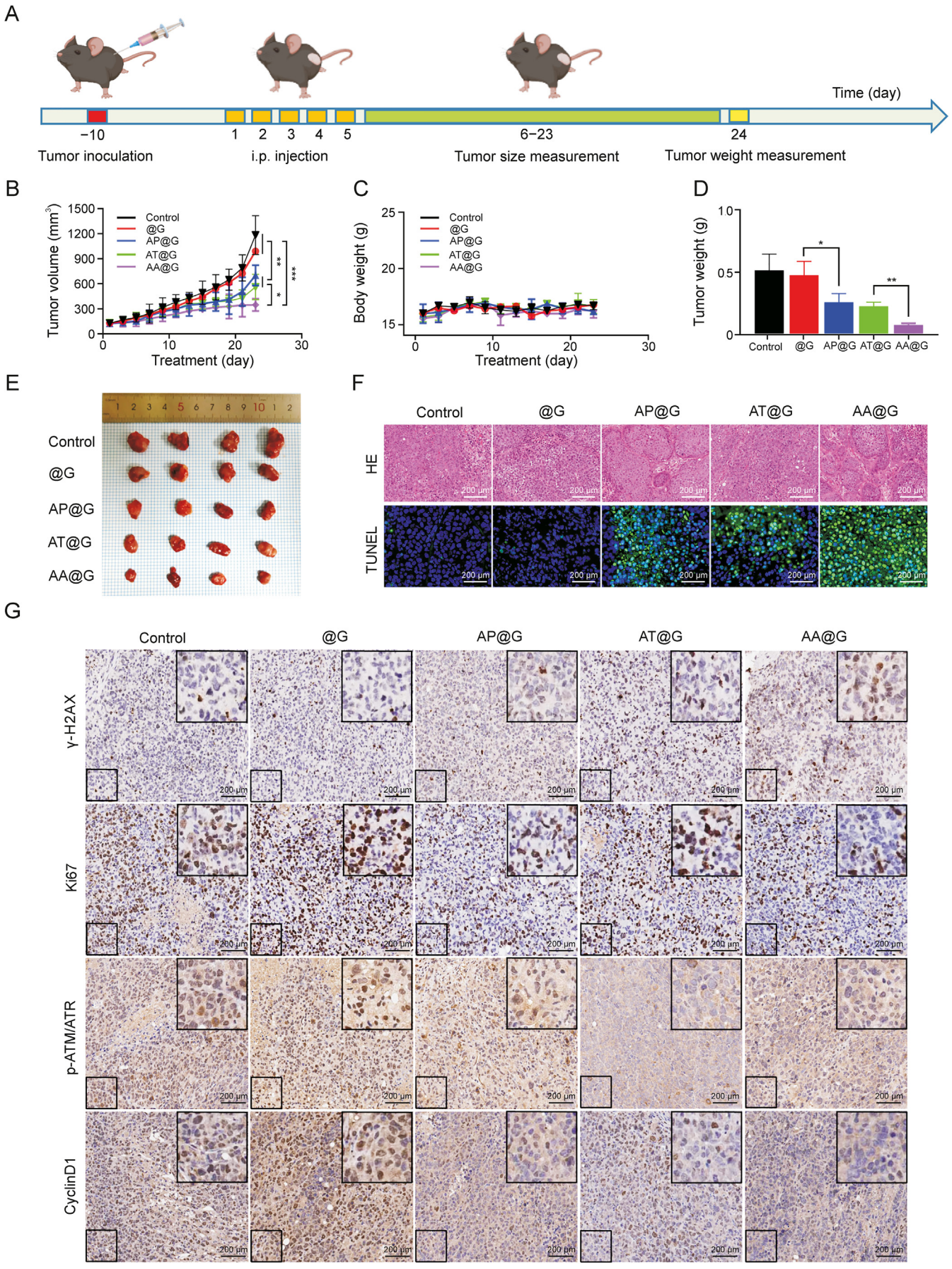
A
Time (day)
−10
1 2 3 4 5
6–23
24
Tumor inoculation
i.p. injection
Tumor size measurement
Tumor weight measurement
B
Tumor volume (mm3)
Treatment (day)
Control
@G
AP@G
AT@G
AA@G
C
Body weight (g)
Treatment (day)
D
Tumor weight (g)
Control
@G
AP@G
AT@G
AA@G
E
F
HE
TUNEL
200 μm
G
γ-H2AX
Ki67
p-ATM/ATR
CyclinD1

certain genes, and can play Gene Ontology (GO) analysis and search Kyoto Encyclopedia of Genes and Genomes (KEGG) signaling pathways of proteins in the protein association network of certain genes [33]. We predicted protein association network of XPO1 and ATR using the STRING, and then conducted GO analysis and KEGG signaling pathways using the STRING database.

3. Results and discussion

3.1. Bioinformatics analysis

The nucleocytoplasmic transport of specific proteins is essential for regulating the cell cycle and cell proliferation, as it can affect important cellular processes, including apoptosis and tumor growth. According to previous studies, various cancer types are associated with elevated levels of XPO1, an important mediator of nucleocytoplasmic transport and cell proliferation, in different cells [34]. Therefore, XPO1 may be considered as a prognostic marker [13] and is a validated drug target in tumor therapies. In this study, we show that XPO1 is significantly overexpressed in liver cancer cells (369 samples) compared to normal cells (50 samples) (Fig. 1A). Survival analysis reveals that the survival time of subjects with high XPO1 expression is shorter than that of subjects with normal XPO1 expression (Fig. 1B). This indicates that XPO1 is a valid therapeutic target in liver cancer patients.

Considering that cycle arrest facilitates the repair of DNA damage induced by the XPO1 inhibitor [16], it is necessary to use other drugs that can inhibit the DNA damage response during the cell cycle. By combining such drugs with the XPO1 inhibitor, the therapeutic efficiency of liver cancer treatments may be significantly improved. Based on the analyses conducted herein, the expression levels of ATR and XPO1 are positively correlated, with a correlation coefficient of 0.54 (Fig. 1C). Like XPO1, the ATR expression in hepatocellular carcinoma patients is higher than that in normal subjects, and the survival time is shorter (Fig. 1D). Knowing that the ATR inhibitor is a superior cell cycle checkpoint inhibitor that can effectively inhibit the DNA damage induced by many types of cancers [17], it can be used in conjunction with the XPO1 inhibitor to treat liver malignancies. The protein association network prediction, GO analysis, and KEGG search performed in this study confirm that the proteins associated with XPO1 and ATR are closely related to cell cycle and DNA damage (Figs. 1E and F). Based on protein structure analysis, AP contain NES. Therefore, this agent can be used to inhibit proteins with NES transport such as XPO1 [35]. Meanwhile, AZD6738 is an ATR inhibitor that effectively inhibits DNA damage repair. In this study, AP and AZD6738 are used as XPO1 and ATR inhibitors, respectively.

3.2. AA@G synthesis and characterization

The @G is widely used in cancer treatment due to its therapeutic efficiency, low toxicity, and deep tumor penetration capacity [31,36–39]. Herein, we use this system as an adjuvant to combine the XPO1 inhibitor (AP) with the ATR inhibitor (AZD6738). The combined preparation is labeled as AA@G. First, AP@G is synthesized from AP, NH_2-PEG_{2000}-SH, and gold nano-adjuvant. Then, AT@G is synthesized by adding the HSA-AZD6738 to the gold nano-adjuvant. At this step, HSA provided a disulfide bond to AZD6738, which could bind to the surface of gold nanoparticles. Finally, AP@G and the HSA-ATR inhibitor are added to the gold nano-adjuvant solution in order to obtain AA@G. As shown in Fig. S1, AP to AZD6738 ratios between 0.5 and 1.25 lead to AP and AZD6738 loading efficiencies in the range of 14%–77% and 11%–81%, respectively. The optimal loading capacities of 77% (AP) and 81% (AZD6738) are obtained at the AP/AZD6738 concentration ratio of 1.

The transmission electron microscope images shown in Fig. 2A demonstrate that @G is composed of spherical nanoparticles with a diameter of 12 nm approximately. The nanoparticles in AP@G, AT@G, and AA@G are nearly spherical; however, their diameters are larger than that of the @G nanoparticles. Elemental mapping analysis shows that Au, S, O, and N elements are scattered on the surface of the AA@G sample (Fig. 2B). These elements are attributed to AP–S–Au, which is formed upon the reduction of Au^{3+} in $HAuCl_4$ by the thiol in AP. It can be seen from the photograph shown in Fig. 2C that all systems investigated herein (@G, AP@G, AT@G, and AA@G) are purple solutions and the @G and AT@G solutions are darker than the AP@G and AA@G solutions. Based on dynamic light scattering analysis, the hydrodynamic diameter of AA@G is about 22.3 nm (Fig. 2D), which is larger than that of @G. Moreover, the zeta potential of this system is up to −21.6 mV (Fig. 2E), whereas that of the @G system is −8.95 mV (Fig. 2F). This indicates that AA@G is more capable of entering cells than @G. As shown in Fig. 2G, the ultraviolet-visible spectroscopy (UV-vis) spectrum of AA@G exhibits the characteristic absorption peaks of AP and AZD6738 (250, 320, and 530 nm), indicating that both agents are successfully loaded into @G (Fig. 2G). This is consistent with the fourier transform infrared spectroscopy results presented in Fig. 2H. Overall, the analytical data discussed above confirm that AA@G has been successfully prepared.

Stability and controllability are essential characteristics of antitumor drug formulations [22,30]. Herein, we hypothesize that AA@G remains stable as it circulates in the blood and that the gold nanoparticles decompose at the target cells to release the therapeutic agents AP and AZD6738. The decomposition of the AA@G system is triggered by high concentrations of GSH, a peptide that can promote the decomposition of gold nanoparticles [40], in tumor cells [41]. To confirm the stability of AA@G in blood circulation, the system was incubated in PBS with 20% fetal bovine serum at pH 7.4 for 24 h, and variations in its hydrodynamic diameter were monitored. As shown in Fig. 2I, the hydrodynamic diameter of AA@G does not change significantly after incubation, which indicates that it remains stable. The GSH-responsive decomposition behavior of AA@G was also tested, and the results presented in Fig. 2I demonstrate that the hydrodynamic diameter of the system decreases quickly after adding 10 mM GSH. Fig. 2J demonstrate that the AA@G particles incubated in PBS solution for 12 h do not exhibit AP, regardless of the solution's pH value (6.0 or 7.4). This confirms that the prepared particles remain stable. However, when 10 mM GSH is added to the incubation solution, an obvious AP is detected in incubated AA@G sample. Based on the spectra recorded at different times during incubation, the release rate of AP reaches 100% within 8 h. A similar release rate is detected for AZD6738 (Fig. S2). Overall, the results prove that AA@G has good stability in blood circulation and that the drugs are only released at the tumor site, where the concentration of GSH is high.

Fig. 6. Treatment effect of gold nano drug carrier loaded AZD6738 and 97–110 amino acids of apoptin (AP) (AA@G) in vivo. (A) Treatment illustration design, mice in different groups were treated with control (PBS), gold nano drug carrier (@G), gold nano drug carrier loaded AP (AP@G), gold nano drug carrier loaded AZD6738 (AT@G), and AA@G ($n = 5$). (B) Tumor volumes in each group ($n = 5$). (C) Body weight of every mouse in each group ($n = 5$). (D) Tumor weight of every mouse in each group ($n = 5$). (E) Photographs of tumor in each group. (F) Hematoxylin-eosin staining (H&E) and terminal deoxynucleotidyl transferase-mediated dUTP nick end labeling (TUNEL) staining in each group ($n = 3$). (G) Immunohistochemistry analysis of γ-H2AX, Ki67, p-ATM/ATR, and CyclinD1 in each group ($n = 3$). $^{*}P < 0.05$; $^{**}P < 0.01$; and $^{***}P < 0.001$. ATM: ataxia telangiectasia-mutated gene.

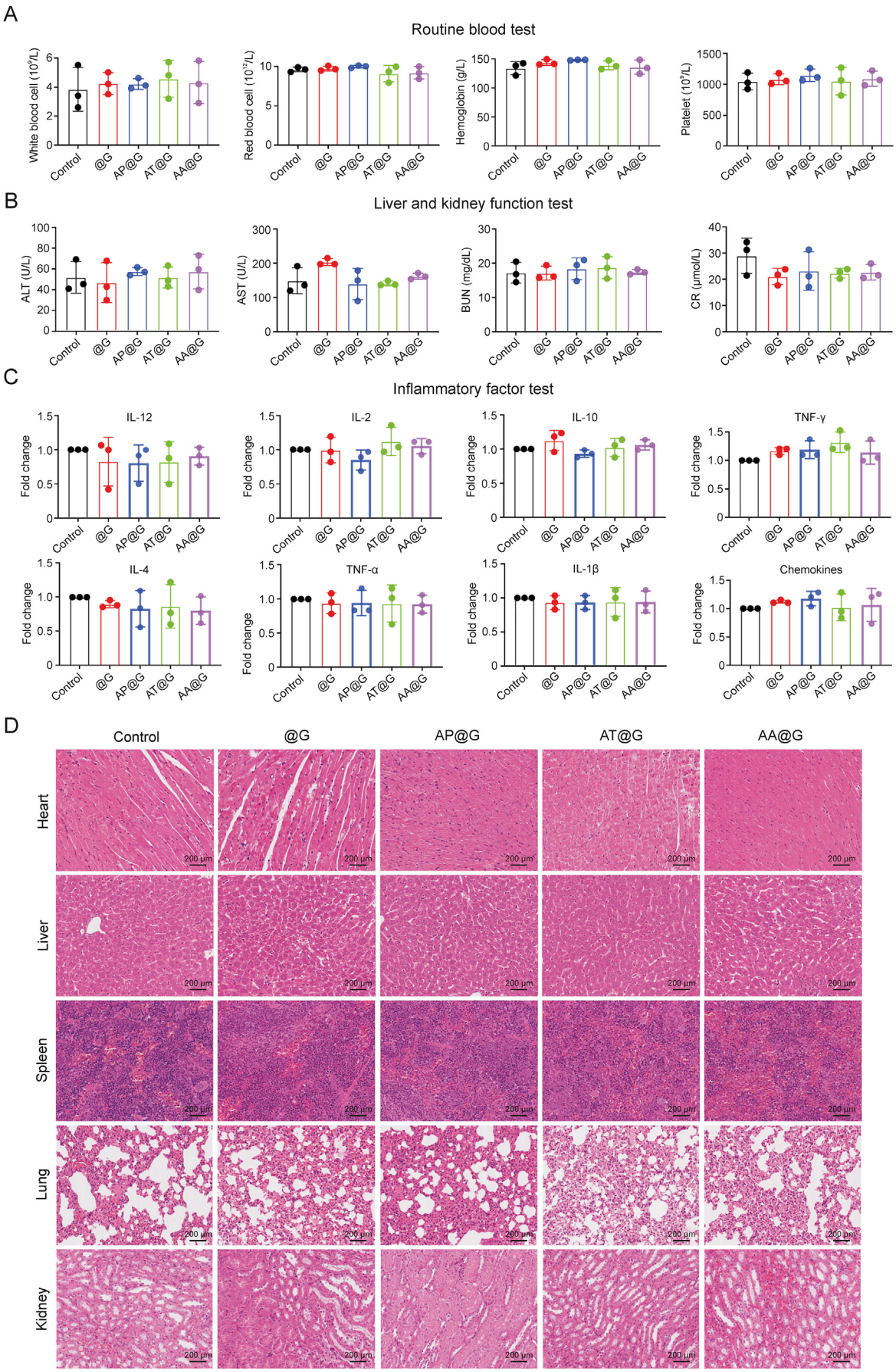
A
Routine blood test
White blood cell (10⁹/L)
Red blood cell (10¹²/L)
Hemoglobin (g/L)
Platelet (10⁹/L)
B
Liver and kidney function test
ALT (U/L)
AST (U/L)
BUN (mg/dL)
CR (μmol/L)
C
Inflammatory factor test
IL-12
IL-2
IL-10
TNF-γ
IL-4
TNF-α
IL-1β
Chemokines
Fold change
Control
@G
AP@G
AT@G
AA@G
D
Heart
Liver
Spleen
Lung
Kidney
200 μm

3.3. Cellular uptake of AA@G

Based on the enhanced permeability and retention (EPR) effect, nanomaterial drug delivery systems (NDDSs) passively accumulate at the tumor site, and thus, do not affect normal tissues [42]. The gold nanoparticles typically used as carrier in NDDSs have superior EPR effect [43], and thus, they are used as an adjuvant in this study to ensure passive targeting of AA@G. To confirm the targeting efficiency of AA@G, experiments were conducted wherein Cy5 was coupled to AP and AZD6738 to form AP-AZD6738-Cy5 or to AA@G to form AA@G-Cy5. After incubation with Hep3B cells for 6 h, the AA@G-Cy5 group showed a stronger fluorescence signal compared to both the control group and the AP-AZD6738-Cy5 group (Fig. 3A). Indeed, most Hep3B cells incubated with AA@G-Cy5 showed obvious red fluorescence after 4 h. Based on flow cytometry analysis, the percentage of fluorescent cells in the AA@G-Cy5 group reached 61.78% and 71.41% after 4 and 6 h of incubation, respectively, which is significantly higher than the percentage detected in the AP-AZD6738-Cy5 group (1.51%) (Fig. 3B).

Since 3D cell spheroids are proposed as better mimics of tumors in vivo [44], the penetrability of AA@G into solid tumor tissues was investigated using 90 μm 3D Hep3B cell spheroids. After incubation with AP-AZD6738-cy5 or AA@G-cy5 for 6 h, the cells were observed by laser scanning confocal microscopy. Based on the results presented in Fig. 3C, both groups of cells show maximum fluorescence at approximately 40 μm away from the spheroid center. The fluorescence intensity decreases at distances closer to the center, indicating that the gold adjuvant promotes the penetration of the AP and AZD6738 drugs into simulated solid tumor.

To assess the in vivo distribution of AA@G, Hep1-6 tumor-bearing C57 mice were injected with AA@G particles; then, the content of AA@G in tumors and organs was determined by measuring ^{197}Au using inductively coupled plasma mass spectrometry. The obtained results show that AA@G is detected in tumors at 6 h after injection and that it accumulates in the tumor tissue for up to 72 h (Fig. 3D). AA@G is also detected in the liver, spleen, and lung at 6 h; however, it is almost undetectable at 72 h (Fig. 3D). This indicates that AA@G is gradually excreted from the body and that it does not accumulate in normal tissues. The tumor-to-organ distribution ratio of ^{197}Au increases significantly over time, which confirms the tumor-targeting ability of AA@G (Fig. 3E). These results demonstrate that AA@G can effectively target tumors and is readily cleared from the body.

3.4. Therapeutic efficacy and mechanism of AA@G in vitro

The therapeutic efficacy of AA@G against four liver cancer cell lines (Hepg2, Hep3B, Huh7, and Hep1-6) was evaluated using the Cell Counting Kit-8 (CCK-8) assay. The results show that treatment with AA@G significantly inhibits the viability of the tested cells; however, the cell viability inhibition ability of free combination of AP and ATR inhibitor (AZD6738) is even inferior to AT@G (Fig. S3), because AP is a short peptide, which cannot enter the cell without transmembrane penetrating peptide modification, and the carrier @G has a therapeutic auxiliary effect [31,36–39]. In addition, treatment with AP@G or AT@G has minimal effect on cell viability (Fig. 4A). The effect of the combined drug formulation was further analyzed using the King's formula: $q = E_{A+B}/(E_A + E_B - E_A \times E_B)$, where E_A, E_B, and E_{A+B} are the inhibition rates of drug A, drug B, and the combined drugs, respectively. If $q < 1$, the drug combination has an antagonistic effect; if $q \geq 1$, the drug combination has a synergistic effect. As shown in Fig. 4B, the q values calculated for Hepg2, Hep3B, Huh7, and Hep1-6 cells are all greater than 1, indicating that AP and AZD6738 exhibit synergistic therapeutic effects. To assess the interaction of AP with AZD6738, the CDI [45] was also calculated using the following formula: CDI = AB/(A × B), where A, B, and AB represent the absorbance ratios of the drug A, drug B, and combined drug (AB) groups, respectively, to the control group at 450 nm. CDI values less than 1 indicate that the two drugs are synergistic, and the synergy is highly significant if CDI < 0.7. As shown in Fig. 4C, all cells treated with AA@G yield CDI < 1, with some groups having CDI < 0.7, except for the Huh7 cells incubated with AP and AZD6738 at the highest drug concentrations. Knowing that Huh7 is a hepatoma cell line with p53 mutation, it may be concluded that this mutation is not conducive to tumor treatment.

Fig. 4D showed the apoptotic rate detected for the AA@G treatment group (47.37%) is significantly higher than the rates detected for the AP@G (24.51%), AT@G group (27.07%), and control (4.64%) groups, and Fig. 4E was the statistical result of three independent repeated cell apoptosis experiment, indicating that AA@G improved the apoptotic rate of liver cancer cells, which is consistent with the CCK-8 assay results. Flow cytometry evaluation of the cell cycle distribution (Fig. 4F) reveals that all treatment groups exhibit a higher percentage of cells in the G_1 phase than the control group (40.72%). Moreover, the percentage of G_1 phase cells in the AA@G group is 73.07%, which is higher than the corresponding percentages in the AP@G (50.27%) and AT@G (51.93%) groups (Fig. 4G). These results indicate that combined treatment with AP and AZD6738 inhibits G_2/M checkpoint activation in Hep3B cells, thereby blocking the cells in the G_1 phase and arresting cell proliferation. Furthermore, calcein-AM/propidium iodide staining experiments performed on 3D Hep3B cell spheroids demonstrate that nearly all Hep3B cells stained with AM in the control and @G groups exhibit green fluorescence (Fig. 4H). However, only the cells in the AA@G group show strong red fluorescence (Fig. 4H), indicating that the AA@G formulation can effectively improve the curative effects of AP and AZD6738.

To maintain life stability, it is essential to preserve the DNA and repair any damage induced by double strand breaks (DSBs) [46]. However, to suppress the growth of tumors, DNA damage must be promoted, and DNA damage repair must be inhibited. Herein, AA@G was designed to achieve both goals, as it induces DNA damage in liver cancer cells while preventing DNA damage repair (Fig. 5A). To explore the mechanism underlying the effect of AA@G in killing hepatoma cells, WB and immunofluorescence analyses were performed. The WB results illustrated in Fig. 5B demonstrate that the expression level of the DSB marker γ-H2AX increases significantly after AA@G treatment, while the levels of the DNA damage repair proteins Rad51 and p-chk1 significantly decrease. Similarly, the immunofluorescence results reveal that AA@G treatment upregulates γ-H2AX but downregulates Rad51 and p-chk1 (Fig. 5C). This indicates that AA@G can simultaneously improve DNA damage and inhibit DNA repair after DSBs in liver cancer cells (Fig. 5A). Considering that the XPO1 inhibitor AP leads to G_1 phase arrest, the expression level of CyclinD1, a mitogenic sensor that controls cell cycle progression [47], was also analyzed

Fig. 7. Biocompatibility of gold nano drug carrier (@G), gold nano drug carrier loaded 97–110 amino acids of apoptin (AP) (AP@G), gold nano drug carrier loaded AZD6738 (AT@G) and gold nano drug carrier loaded AZD6738 and AP (AA@G) in vivo was evaluated. (A) The changes of white blood cell (WBC), red blood cell (RBC), hemoglobin (HGB), and platelet (PLT). (B) The changes of alanine aminotransferase (ALT), aspartate aminotransferase (AST), blood urea nitrogen (BUN), and creatinine (CR). (C) The changes of concentrations of inflammatory factors in serum. (D) Hematoxylin-eosin staining (H&E) staining of mice after three injections of @G, AP@G, AT@G, and AA@G ($n = 3$).

by WB. As shown in Fig. 5B, AA@G treatment downregulates the expression of CyclinD1. This result is confirmed by immunofluorescence analysis (Fig. 5C), and it indicates that AA@G inhibits the proliferation of cells by blocking them in the G_1 phase (Fig. 5A).

3.5. Therapeutic efficacy and mechanism of AA@G in vivo

To determine the effect of AA@G in vivo, Hep1-6 tumor-bearing mice were randomly divided into different groups and administered with PBS (control group), @G, AP@G, AT@G, or AA@G, as illustrated in Fig. 6A. The tumor volumes and tumor weights of the mice were recorded every two days in order to assess the effects of different treatments. As shown in Fig. 6B, the tumor volumes of mice treated with AP@G, AT@G, and AA@G are smaller than those of the control group mice, and the smallest tumors were detected in AA@G mice. However, the body weights were almost the same in every group (Fig. 6C). A similar trend was observed for tumor weights, with AA@G mice showing the least weights at the end of the experiment, followed by AP@G and AT@G mice, and then the control and @G mice (Fig. 6D). In addition, Fig. 6E showed the photograph of stripped tumor body from control, @G, AP@G, AT@G, and AA@G groups. To confirm the therapeutic efficacy of AA@G, H&E and terminal deoxynucleotidyl transferase-mediated dUTP nick end labeling staining analyses were performed. As shown in Fig. 6F, the necrosis and green dots detected in the AA@G group are greater than those observed for other experimental and control groups, which indicate that AA@G has remarkable therapeutic efficacy in vivo. The mechanism underlying the tumor proliferation inhibition activity of AA@G was determined by immunohistochemical (IHC) staining. The obtained results reveal that AA@G treatment upregulates the expression of the DNA DSB marker γ-H2AX (Fig. 6G), which agrees well with the results of in vitro experiments. This indicates that AA@G promotes DNA damage by increasing the number of DSBs. In addition, it effectively inhibits tumor cell proliferation, as evidenced by Ki67 IHC staining analyses (Fig. 6G). Knowing that the activation of ataxia telangiectasia-mutated gene (ATM) and ATR induces DSB repair and that the inhibition of ATR abrogates the repair of DSBs by HR [17], the effects of different treatments on the expression levels of ATM and ATR in tumor-bearing mice were also examined. As shown in Fig. 6G, AT@G and AA@G treatments downregulate ATM and ATR expression due to the effect of AZD6738 in inhibiting ATR. Meanwhile, the expression level of CyclinD1 in tumor sites is downregulated by AT@G, as well as by AP@G treatment, and it is significantly reduced by AA@G. This indicates that AP@G and AT@G can block cells in the G_1 phase and that the combined drug formula (AA@G) has the best G_1 blocking effect. Based on these results, it may be concluded that AA@G inhibits tumor growth by promoting DNA damage, inhibiting DNA damage repair, promoting G_1 phase arrest, and inhibiting tumor cell proliferation.

3.6. Biocompatibility of AA@G

To determine whether a drug formulation may be applied in clinical treatment, it is essential to evaluate its biosafety [48]. Considering that changes in the behavior and body weights of mice are considered as signs of acute toxicity and that changes in gross pathology reflect long-term toxicity [49], these parameters were assessed throughout the treatment period. Blood samples were collected from mice administered with intraperitoneal injections of PBS, @G, AP@G, AT@G, and AA@G, and the behavior and body weights of these mice were monitored. The results show that treatment with @G, AP@G, AT@G, or AA@G does not induce significant variations in mouse behavior and body weight compared to the control group (Fig. 6C), which proves that the acute toxicity of @G, AP@G, AT@G, and AA@G is low. Similarly, routine blood tests reveal that the PBS- and drug-injected groups do not exhibit any appreciable differences, even after 30 days of treatment (Fig. 7A). This indicates that @G, AP@G, AT@G, and AA@G do not cause hemolysis or myelosuppression. To evaluate any potential liver or kidney damage induced by @G, AP@G, AT@G, and AA@G, liver and kidney function tests were performed. In accordance with previous studies, alanine aminotransferase (ALT) and aspartate aminotransferase (AST) were assessed as liver damage indexes, and blood urea nitrogen (BUN) and creatinine (CR) were assessed as kidney damage indexes [50–52]. The obtained results demonstrate that ALT, AST, BUN, and CR values corresponding to different groups are similar (Fig. 7B), which suggests that @G, AP@G, AT@G, and AA@G do not damage liver and kidney functions. Assessment of the inflammatory factor levels in serum samples collected from mice in different groups shows that these levels do not exhibit significant variation compared to the control group (Fig. 7C), which suggests that treatment with @G, AP@G, AT@G, or AA@G does not cause serious immune inflammatory reaction. Concomitantly, H&E staining analysis reveals that no organ damage is induced by @G, AP@G, AT@G, or AA@G (Fig. 7D). Collectively, the data signify that @G, AP@G, AT@G, and AA@G are highly biocompatible and can potentially be used in clinical treatment.

4. Conclusion

In this study, a super-assembled nano-pill (AA@G) with multiple therapy sensitizations against liver cancer was prepared by loading AZD6738 (ATR small-molecule inhibitor)-binding HSA onto an AP (XPO peptide inhibitor)-Au supramolecular nanoparticle. The obtained results show that AA@G possesses superior biocompatibility and improved therapeutic efficiency compared to other treatments, both in vitro and in vivo. The therapeutic efficacy of AA@G is attributed to its multiple effects, including XPO1 inhibition, ATR inhibition, DNA damage enhancement, DNA damage repair suppression, cell cycle blocking, and apoptosis. Overall, this study provides a co-delivery strategy for the clinical treatment of intensive liver cancer. Moreover, it develops an approach to unify the pharmacokinetics of peptide and small-molecule compounds, thereby extending the scope of drugs used in advanced combination therapy.

CRediT author statement

Liuyun Gong and **Yinliang Lu**: Methodology, Investigation, Software, Writing - Original draft preparation; **Jing Wang** and **Xinyue Li**: Data curation, Methodology; **Jing Zhao** and **Yuetong Chen**: Software, Validation; **Rongze Ma** and **Jinlu Ma**: Writing - Reviewing and Editing; **Tianya Liu** and **Suxia Han**: Conceptualization, Methodology.

Declaration of competing interest

The authors declare that there are no conflicts of interest.

Acknowledgments

This work was supported by the National Natural Science Foundation of China (Grant Nos.: 81272488 and 81602802) and the Shaanxi Province Innovation Capacity Support Program (Grant No.: 2018TD-002). We thank Mr. Xiaofei Wang et al. at the Experimental Biomedical Center of Xi'an Jiaotong University for their kind assistance with the instrument operation and data analysis.

Appendix A. Supplementary data

Supplementary data to this article can be found online at https://doi.org/10.1016/j.jpha.2023.04.017.

References

[1] F. Islami, K.D. Miller, R.L. Siegel, et al., Disparities in liver cancer occurrence in the United States by race/ethnicity and state, CA Cancer J. Clin. 67 (2017) 273–289.

[2] C. Wang, Y. Cao, C. Yang, et al., Exploring liver cancer biology through functional genetic screens, Nat. Rev. Gastroenterol. Hepatol. 18 (2021) 690–704.

[3] C. Wang, H. Jin, D. Gao, et al., Phospho-ERK is a biomarker of response to a synthetic lethal drug combination of sorafenib and MEK inhibition in liver cancer, J. Hepatol. 69 (2018) 1057–1065.

[4] C. Xu, Y. Zhang, P.A. Rolfe, et al., Combination therapy with NHS-muIL12 and avelumab (anti-PD-L1) enhances antitumor efficacy in preclinical cancer models, Clin. Cancer Res. 23 (2017) 5869–5880.

[5] A. Montinaro, I. Areso Zubiaur, J. Saggau, et al., Potent pro-apoptotic combination therapy is highly effective in a broad range of cancers, Cell Death Differ. 29 (2022) 492–503.

[6] J. She, Y. Li, S. Yan, et al., *De novo* supraparticle construction by a self-assembled Janus cyclopeptide to tame hydrophilic microRNA and hydrophobic molecule for anti-tumor cocktail therapy and augmented immunity, Chem. Eng. J. 401 (2020), 126080.

[7] Q. Hu, W. Sun, C. Wang, et al., Recent advances of cocktail chemotherapy by combination drug delivery systems, Adv. Drug Deliv. Rev. 98 (2016) 19–34.

[8] H.S. Han, B.K. Arun, B. Kaufman, et al., Veliparib monotherapy following carboplatin/paclitaxel plus veliparib combination therapy in patients with germline *BRCA*-associated advanced breast cancer: Results of exploratory analyses from the phase III BROCADE3 trial, Ann. Oncol. 33 (2022) 299–309.

[9] J. Guo, L. Huang, Formulation of two lipid-based membrane-core nanoparticles for FOLFOX combination therapy, Nat. Protoc. 17 (2022) 1818–1831.

[10] J. Niu, C. Maurice-Dror, D.H. Lee, et al., First-in-human phase 1 study of the anti-TIGIT antibody vibostolimab as monotherapy or with pembrolizumab for advanced solid tumors, including non-small-cell lung cancer, Ann. Oncol. 33 (2022) 169–180.

[11] T. Hank, M. Sandini, C.R. Ferrone, et al., A combination of biochemical and pathological parameters improves prediction of postresection survival after preoperative chemotherapy in pancreatic cancer: The PANAMA-score, Ann. Surg. 275 (2022) 391–397.

[12] M. Zhang, P. Gong, L. Ge, et al., Nuclear exportin 1 (XPO1) binds to the nuclear localization/export signal of the turnip mosaic virus Nlb to promote viral infection, Front. Microbiol. 12 (2022), 780724.

[13] J. Kim, E. McMillan, H.S. Kim, et al., XPO1-dependent nuclear export is a druggable vulnerability in KRAS-mutant lung cancer, Nature 538 (2016) 114–117.

[14] O. Podlaha, M. Riester, S. De, et al., Evolution of the cancer genome, Trends Genet. 28 (2012) 155–163.

[15] P. Lito, N. Rosen, D.B. Solit, Tumor adaptation and resistance to RAF inhibitors, Nat. Med. 19 (2013) 1401–1409.

[16] A. Inoue, F.S. Robinson, R. Minelli, et al., Sequential administration of XPO1 and ATR inhibitors enhances therapeutic response in *TP53*-mutated colorectal cancer, Gastroenterology 161 (2021) 196–210.

[17] B. Haynes, J. Murai, J.M. Lee, Restored replication fork stabilization, a mechanism of PARP inhibitor resistance, can be overcome by cell cycle checkpoint inhibition, Cancer Treat. Rev. 71 (2018) 1–7.

[18] Q. Shi, L.-Y. Shen, B. Dong, et al., The identification of the ATR inhibitor VE-822 as a therapeutic strategy for enhancing cisplatin chemosensitivity in esophageal squamous cell carcinoma, Cancer Lett. 432 (2018) 56–68.

[19] W. He, J. Yan, F. Sui, et al., Turning a *Luffa* protein into a self-assembled biodegradable nanoplatform for multitargeted cancer therapy, ACS Nano 12 (2018) 11664–11677.

[20] W. He, S. Wang, J. Yan, et al., Self-assembly of therapeutic peptide into stimuli-responsive clustered nanohybrids for cancer-targeted therapy, Adv. Funct. Mater. 29 (2019), 1807736.

[21] J. Yan, S. Yan, P. Hou, et al., A hierarchical peptide-lanthanide framework to accurately redress intracellular carcinogenic protein-protein interaction, Nano Lett. 19 (2019) 7918–7926.

[22] W. Yang, W. Liu, X. Li, et al., Turning chiral peptides into a racemic supraparticle to induce the self-degradation of MDM2, J. Adv. Res. 45 (2023) 59–71.

[23] W. He, J. Yan, Y. Li, et al., Resurrecting a p53 peptide activator - An enabling nanoengineering strategy for peptide therapeutics, J. Control. Release 325 (2020) 293–303.

[24] J. Yan, F. Ji, S. Yan, et al., A general-purpose nanohybrid fabricated by polymeric Au(I)-peptide precursor to wake the function of peptide therapeutics, Theranostics 10 (2020) 8513–8527.

[25] Z. Bian, J. Yan, S. Wang, et al., Awakening p53 *in vivo* by D-peptides-functionalized ultra-small nanoparticles: Overcoming biological barriers to D-peptide drug delivery, Theranostics 8 (2018) 5320–5335.

[26] W. He, Z. Zhang, W. Yang, et al., Turing milk into pro-apoptotic oral nanotherapeutic: *De novo* bionic chiral-peptide supramolecule for cancer targeted and immunological therapy, Theranostics 12 (2022) 2322–2334.

[27] L. Li, W. He, W. You, et al., Turing miRNA into infinite coordination supermolecule: A general and enabling nanoengineering strategy for resurrecting nuclear acid therapeutics, J. Nanobiotechnology 20 (2022), 10.

[28] S. Yan, J. Yan, D. Liu, et al., A nano-predator of pathological MDMX construct by clearable supramolecular gold(I)-thiol-peptide complexes achieves safe and potent anti-tumor activity, Theranostics 11 (2021) 6833–6846.

[29] W. He, J. Yan, L. Wang, et al., A lanthanide-peptide-derived bacterium-like nanotheranostic with high tumor-targeting, -imaging and -killing properties, Biomaterials 206 (2019) 13–24.

[30] J. Yan, Y. Yao, S. Yan, et al., Chiral protein supraparticles for tumor suppression and synergistic immunotherapy: An enabling strategy for bioactive supramolecular chirality construction, Nano Lett. 20 (2020) 5844–5852.

[31] A. Chen, L. Wu, Y. Luo, et al., Deep tumor penetrating gold nano-adjuvant for NIR-II-triggered *in situ* tumor vaccination, Small 18 (2022), e2200993.

[32] L. Gong, Y. Zhang, J. Zhao, et al., All-in-one biomimetic nanoplatform based on hollow polydopamine nanoparticles for synergistically enhanced radiotherapy of colon cancer, Small 18 (2022), e2107656.

[33] X. Sun, Z. Luo, L. Gong, et al., Identification of significant genes and therapeutic agents for breast cancer by integrated genomics, Bioengineered 12 (2021) 2140–2154.

[34] G.L. Gravina, W. Senapedis, D. McCauley, et al., Nucleo-cytoplasmic transport as a therapeutic target of cancer, J. Hematol. Oncol. 7 (2014), 85.

[35] J. Wang, J. Zhao, F. Ma, et al., One stone, two birds: A peptide-Au(I) infinite coordination supermolecule for the confederate physical and biological radiosensitization in cancer radiation therapy, Small 19 (2023), e2204238.

[36] R. Han, L.W.C. Ho, Q. Bai, et al., Alkyl-terminated gold nanoparticles as a self-therapeutic treatment for psoriasis, Nano Lett. 21 (2021) 8723–8733.

[37] L. Xu, Y. Liu, Z. Chen, et al., Surface-engineered gold nanorods: Promising DNA vaccine adjuvant for HIV-1 treatment, Nano Lett. 12 (2012) 2003–2012.

[38] H.S. Han, K.Y. Choi, H. Lee, et al., Gold-nanoclustered hyaluronan nano-assemblies for photothermally maneuvered photodynamic tumor ablation, ACS Nano 10 (2016) 10858–10868.

[39] S.A.C. Carabineiro, Applications of gold nanoparticles in nanomedicine: Recent advances in vaccines, Molecules 22 (2017), 857.

[40] L. Kennedy, J.K. Sandhu, M.E. Harper, et al., Role of glutathione in cancer: From mechanisms to therapies, Biomolecules 10 (2020), 1429.

[41] K. Ock, W.I. Jeon, E.O. Ganbold, et al., Real-time monitoring of glutathione-triggered thiopurine anticancer drug release in live cells investigated by surface-enhanced Raman scattering, Anal. Chem. 84 (2012) 2172–2178.

[42] Z. Zhang, Q. Deng, C. Xiao, et al., Rational design of nanotherapeutics based on the five features principle for potent elimination of cancer stem cells, Acc. Chem. Res. 55 (2022) 526–536.

[43] M.I. Setyawati, C.Y. Tay, B.H. Bay, et al., Gold nanoparticles induced endothelial leakiness depends on particle size and endothelial cell origin, ACS Nano 11 (2017) 5020–5030.

[44] L. Kou, Q. Yao, S. Sivaprakasam, et al., Dual targeting of L-carnitine-conjugated nanoparticles to OCTN2 and $ATB^{0,+}$ to deliver chemotherapeutic agents for colon cancer therapy, Drug Delivery 24 (2017) 1338–1349.

[45] L. Liu, X. Xiong, M. Shen, et al., Co-delivery of triptolide and curcumin for ovarian cancer targeting therapy via mPEG-DPPE/CaP nanoparticle, J. Biomed. Nanotechnol. 14 (2018) 1761–1772.

[46] Y. Dong, D. Zhang, M. Cai, et al., SPOP regulates the DNA damage response and lung adenocarcinoma cell response to radiation, Am. J. Cancer Res. 9 (2019) 1469–1483.

[47] G. Tchakarska, B. Sola, The double dealing of cyclin D1, Cell Cycle 19 (2020) 163–178.

[48] F. Zor, F.N. Selek, G. Orlando, et al., Biocompatibility in regenerative nanomedicine, Nanomedicine (Lond) 14 (2019) 2763–2775.

[49] M.S. Malayappan, G. Natarajan, L. Mockaiyathevar, et al., Acute and subacute toxicity assessment of Madhulai Manappagu (Siddha herbal syrup formulation) in animal model, J. Complement. Integr. Med. 19 (2021) 9–18.

[50] A. Parker, Y. Kim, The effect of low glycemic index and glycemic load diets on hepatic fat mass, insulin resistance, and blood lipid panels in individuals with nonalcoholic fatty liver disease, Metab. Syndr. Relat. Disord. 17 (2019) 389–396.

[51] J. Zhou, Z. He, S. Ma, et al., AST/ALT ratio as a significant predictor of the incidence risk of prostate cancer, Cancer Med. 9 (2020) 5672–5677.

[52] A. Cai, S. Qi, Z. Su, et al., Method comparison and bias estimation of blood urea nitrogen (BUN), creatinine (Cr), and uric acid (UA) measurements between two analytical methods, Clin. Lab. 63 (2017) 73–77.